

**OPEN ACCESS**

## Performance Projection of a High-Temperature CO<sub>2</sub> Transport Membrane Reactor for Combined CO<sub>2</sub> Capture and Methane-to-Ethylene Conversion

To cite this article: Xin Li *et al* 2022 *J. Electrochem. Soc.* **169** 053501

View the [article online](#) for updates and enhancements.

**Measure the electrode expansion in the nanometer range.**  
**Discover the new electrochemical dilatometer ECD-4-nano!**

**EL-CELL®**  
electrochemical test equipment



- PAT series test cell for dilatometric analysis (expansion of electrodes)
- Capacitive displacement sensor (range 250 µm, resolution ≤ 5 nm)
- Optimized sealing concept for high cycling stability

[www.el-cell.com](http://www.el-cell.com) +49 (0) 40 79012 737 [sales@el-cell.com](mailto:sales@el-cell.com)





# Performance Projection of a High-Temperature CO<sub>2</sub> Transport Membrane Reactor for Combined CO<sub>2</sub> Capture and Methane-to-Ethylene Conversion

Xin Li,<sup>1</sup> Kevin Huang,<sup>1</sup>  Noah Van Dam,<sup>2</sup> and Xinfang Jin<sup>2,z</sup> 

<sup>1</sup> Mechanical Engineering Department, University of South Carolina, Columbia, South Carolina 29201, United States of America

<sup>2</sup> Mechanical Engineering Department, University of Massachusetts, Lowell, Massachusetts 01854, United States of America

Direct conversion of methane into ethylene through the oxidative coupling of methane (OCM) is a technically important reaction. However, conventional co-fed fixed-bed OCM reactors still face serious challenges in conversion and selectivity. In this paper, we apply a finite element model to simulate OCM reaction in a plug-flow CO<sub>2</sub>/O<sub>2</sub> transport membrane (CTM) reactor with a directly captured CO<sub>2</sub> and O<sub>2</sub> mixture as a soft oxidizer. The CTM is made of three phases: molten carbonate, 20% Sm-doped CeO<sub>2</sub>, and LiNiO<sub>2</sub>. The membrane parameters are first validated by CO<sub>2</sub>/O<sub>2</sub> flux data obtained from CTM experiments. The OCM reaction is then simulated along the length of tubular plug-flow reactors filled with a La<sub>2</sub>O<sub>3</sub>-CaO-modified CeO<sub>2</sub> catalyst bed, while a mixture of CO<sub>2</sub>/O<sub>2</sub> is gradually added through the wall of the tubular membrane. A 12-step OCM kinetic mechanism is considered in the model for the catalyst bed and validated by data obtained from a co-fed fixed-bed reactor. The modeled results indicate a much-improved OCM performance by membrane reactor in terms of C<sub>2</sub>-yield and CH<sub>4</sub> conversion rate over the state-of-the-art, co-fed, fixed-bed reactor. The model further reveals that improved performance is fundamentally rooted in the gradual methane conversion with CO<sub>2</sub>/O<sub>2</sub> offered by the plug-flow membrane reactor.

© 2022 The Author(s). Published on behalf of The Electrochemical Society by IOP Publishing Limited. This is an open access article distributed under the terms of the Creative Commons Attribution 4.0 License (CC BY, <http://creativecommons.org/licenses/by/4.0/>), which permits unrestricted reuse of the work in any medium, provided the original work is properly cited. [DOI: [10.1149/1945-7111/ac6ae7](https://doi.org/10.1149/1945-7111/ac6ae7)]



Manuscript submitted February 2, 2022; revised manuscript received March 25, 2022. Published May 9, 2022. *This paper is part of the JES Focus Issue on Electrochemical Separations and Sustainability.*

## List of symbols

Symbols	Unit	Physical Meaning
c	mol m <sup>-3</sup>	Molar fraction
D	m <sup>2</sup> s <sup>-1</sup>	Diffusion coefficient
Ea	J mol <sup>-1</sup>	Activation energy in the reaction step j
F		Faraday's constant
ΔH	J mol <sup>-1</sup>	Enthalpy
J	A cm <sup>-2</sup>	Current
k		Pre-exponential factor
K	Pa <sup>-1</sup>	Adsorption constant
m,n		Reaction order
N	mol m <sup>-2</sup> s <sup>-1</sup>	Molar Flux
P	Pa	Partial pressure
R	J/(mol·K)	Gas constant
T	K	Temperature
Z		Charge
Greek Symbols		
ε		Volume fraction of molten carbonate
σ	S m <sup>-1</sup>	Conductivity
Φ	V	Electric potential
μ	J mol <sup>-1</sup>	Chemical potential
τ		Tortuosity
Subscripts and superscripts		
ad		adsorption
C		Carbonate ion
D		Cation defect
e		Electron in metal phase
n		Electron in solid oxide phase
MC		Molten carbonate phase
LNO		LiNiO <sub>2</sub> phase
V		Oxide vacancy

A recent notable development in the energy field is the significantly increased production of natural gas (NG) from shale and tight oil.<sup>1</sup> If the newly available, low-cost NG is only used for producing heat and power as in the past, it will continue to emit a significant amount of CO<sub>2</sub> into the atmosphere and add burdens to the current effort to mitigate global warming and climate change issues.<sup>2,3</sup> Alternatively, NG can be directly converted into value-added products with minimal CO<sub>2</sub> emissions.<sup>4</sup> This direct methane conversion (DMC) approach is also economically attractive due to higher economic values of the final products.<sup>5,6</sup>

The most studied DMC technology is Oxidative Coupling of Methane (OCM), transforming CH<sub>4</sub> into ethylene (C<sub>2</sub>H<sub>4</sub>) with molecular O<sub>2</sub> as the oxidant in a single step.<sup>7</sup> A major technical challenge for the OCM process is to achieve high CH<sub>4</sub> conversion at high C<sub>2</sub> selectivity.<sup>8</sup> A number of new reactor designs have been proposed based on the concept of controlling the oxygen content to prevent over-oxidation of the desirable C<sub>2</sub> products.<sup>9</sup>

From a design perspective, there are generally three types of reactors: moving or fluidized-bed reactor, fixed-bed reactor, and membrane reactor.<sup>10,11</sup> For the moving or fluidized bed reactors, the solid catalysts need to be replenished at a high frequency in order to remove coke and achieve a C<sub>2</sub> yield greater than 50%.<sup>12,13</sup> However, it is energy intensive to invest in larger reactor vessels, regenerate a large amount of solid catalyst, and provide high pumping power to move the catalyst. For fixed-bed reactors, there is little control over the over-oxidation of C<sub>2</sub> such that C<sub>2</sub> yield is often limited to <25%.<sup>14</sup> There were some proposed fixed-bed reactors with the ability to control the oxygen concentration in a continuous reactor by distributing the oxygen feed during the reaction to reduce the over-oxidation of C<sub>2</sub> products. But, distributing oxygen feed in a reactor is not trivial and could become very costly.<sup>15</sup> The membrane reactors reported in the open literature are either porous membrane reactors or membrane reactors with solid-oxide O<sub>2</sub> transport materials (OTMs).<sup>16,17</sup> However, the improvement in C<sub>2</sub> yield and selectivity demonstrated so far is still marginal.<sup>18</sup>

To control oxygen concentration, previous studies have shown that using nitrogen oxide, carbon dioxide, or sulfur as a soft oxidizer can appreciably improve the conversion-selectivity relationship.<sup>19</sup> Here in this study, we investigate from a modeling perspective the performance of a membrane reactor to directly convert methane to ethylene via OCM using a mixture of CO<sub>2</sub>/O<sub>2</sub>. In this case, a multi-

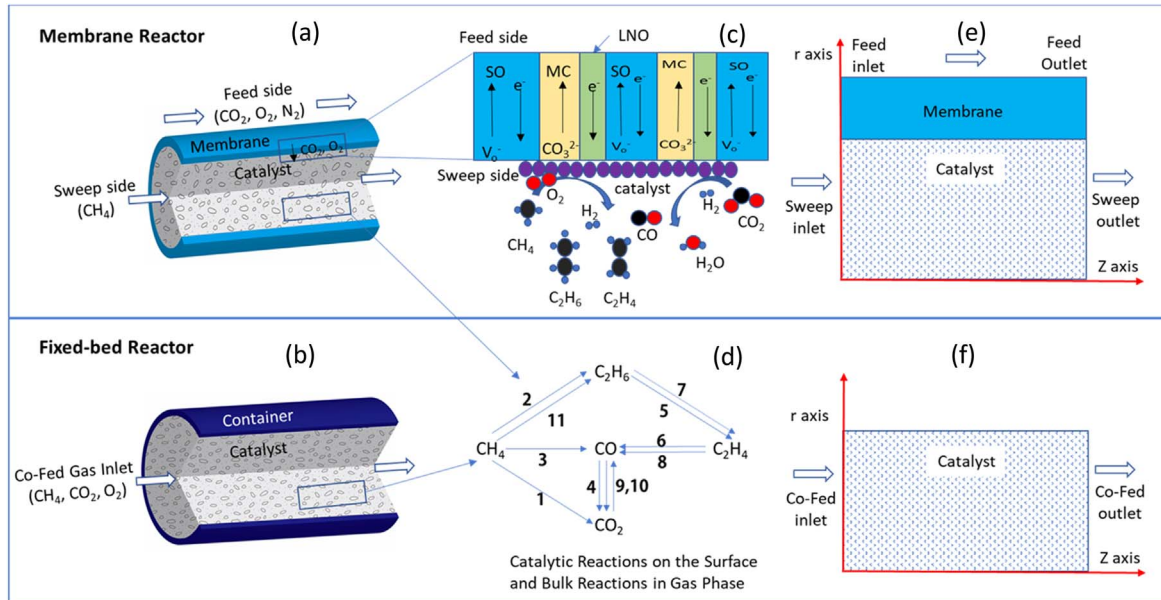


**Figure 1.** Schematic Illustration of (a) Membrane reactor; (b) Co-fed fixed bed reactor. (c) charge species transport and surface reactions in the membrane reactor. (d) Reaction pathway diagram. (Numbers correspond to reaction indexes given in Table I). 2D axial symmetric computational domain of (e) Membrane reactor; (f) Co-fed fixed bed reactor.

**Table I. Reactions and Kinetic Rates.<sup>21</sup>**

Index	Reaction	Reaction Kinetics
1	CH <sub>4</sub> + 2O <sub>2</sub> → CO <sub>2</sub> + 2H <sub>2</sub> O	$r_1 = \frac{(k_{01} \cdot e^{-\frac{E_a}{RT}}) \cdot P_{CH_4}^{m_1} \cdot P_{O_2}^{n_1} - k_b v e^{-\frac{E_a}{RT}} \cdot P_{CO_2}^{m_1} \cdot P_{H_2O}^{n_1}}{(1 + K_{1,CO_2} \cdot e^{-\frac{\Delta H_{ad,CO_2,1}}{RT}} \cdot P_{CO_2})^2}$
2	2CH <sub>4</sub> + 0.5O <sub>2</sub> → C <sub>2</sub> H <sub>6</sub> + H <sub>2</sub> O	$r_2 = \frac{k_{02} \cdot e^{-\frac{E_a}{RT}} \cdot (K_{0O_2} \cdot e^{-\frac{\Delta H_{ad,O_2}}{RT}} \cdot P_{O_2})^{n_2} \cdot P_{CH_4}}{\left[ 1 + (K_{0,O_2} \cdot e^{-\frac{\Delta H_{ad,O_2}}{RT}} \cdot P_{O_2})^n + K_{2,CO_2} \cdot e^{-\frac{\Delta H_{ad,O_2}}{RT}} \cdot P_{O_2} \right]^2}$
3	CH <sub>4</sub> + O <sub>2</sub> → CO + H <sub>2</sub> O + H <sub>2</sub>	$r_3 = \frac{(k_{03} \cdot e^{-\frac{E_a}{RT}}) \cdot P_{CH_4}^{m_3} \cdot P_{O_2}^{n_3} - k_b \cdot e^{-\frac{E_a}{RT}} \cdot P_{CO_2}^{m_3} \cdot P_{H_2O}^{n_3}}{(1 + K_{3,CO_2} \cdot e^{-\frac{\Delta H_{ad,CO_2,3}}{RT}} \cdot P_{CO_2})^2}$
4	CO + 0.5O <sub>2</sub> → CO <sub>2</sub>	$r_4 = \frac{(k_{04} \cdot e^{-\frac{E_a}{RT}}) \cdot P_{CH_4}^{m_4} \cdot P_{O_2}^{n_4} - k_b \cdot e^{-\frac{E_a}{RT}} \cdot P_{CO_2}^{m_4} \cdot P_{H_2O}^{n_4}}{(1 + K_{4,CO_2} \cdot e^{-\frac{\Delta H_{ad,CO_2,4}}{RT}} \cdot P_{CO_2})^2}$
5	C <sub>2</sub> H <sub>6</sub> + 0.5O <sub>2</sub> → C <sub>2</sub> H <sub>4</sub> + H <sub>2</sub> O	$r_5 = \frac{(k_{05} \cdot e^{-\frac{E_a}{RT}}) \cdot P_{CH_4}^{m_5} \cdot P_{O_2}^{n_5} - k_b \cdot e^{-\frac{E_a}{RT}} \cdot P_{CO_2}^{m_5} \cdot P_{H_2O}^{n_5}}{(1 + K_{5,CO_2} \cdot e^{-\frac{\Delta H_{ad,CO_2,5}}{RT}} \cdot P_{CO_2})^2}$
6	C <sub>2</sub> H <sub>4</sub> + 2O <sub>2</sub> → 2CO + 2H <sub>2</sub> O	$r_6 = \frac{(k_{06} \cdot e^{-\frac{E_a}{RT}}) \cdot P_{CH_4}^{m_6} \cdot P_{O_2}^{n_6} - k_b \cdot e^{-\frac{E_a}{RT}} \cdot P_{CO_2}^{m_6} \cdot P_{H_2O}^{n_6}}{(1 + K_{6,CO_2} \cdot e^{-\frac{\Delta H_{ad,CO_2,6}}{RT}} \cdot P_{CO_2})^2}$
7	C <sub>2</sub> H <sub>6</sub> → C <sub>2</sub> H <sub>4</sub> + H <sub>2</sub>	$r_7 = k_{07} \cdot e^{-\frac{E_a}{RT}} \cdot P_{C_2H_6}$
8	C <sub>2</sub> H <sub>4</sub> + 2H <sub>2</sub> O → 2CO + 4H <sub>2</sub>	$r_8 = k_{08} \cdot e^{-\frac{E_a}{RT}} \cdot P_{C_2H_4}^{m_8} \cdot P_{H_2O}^{n_8}$
9	CO + H <sub>2</sub> O → CO <sub>2</sub> + H <sub>2</sub>	$r_9 = k_{09} \cdot e^{-\frac{E_a}{RT}} \cdot P_{CO}^{m_9} \cdot P_{H_2O}^{n_9}$
10	CO <sub>2</sub> + H <sub>2</sub> → CO + H <sub>2</sub> O	$r_{10} = k_{10} \cdot e^{-\frac{E_a}{RT}} \cdot P_{CO_2}^{m_{10}} \cdot P_{H_2O}^{n_{10}}$
11	2CH <sub>4</sub> + CO <sub>2</sub> → C <sub>2</sub> H <sub>6</sub> + H <sub>2</sub> O + CO	$r_{11} = k_{11} \cdot e^{-\frac{E_a}{RT}} \cdot P_{CH_4}^{m_{11}} \cdot P_{CO_2}^{n_{11}}$

phase, high-temperature CO<sub>2</sub> transport membrane (CTM) is used to separate CO<sub>2</sub> and O<sub>2</sub> from a carbon source such as flue gas and simultaneously react with methane on the other side of the membrane to form ethylene in the presence of OCM catalysts. We combine experimental data from the most recent CTM study and

reaction kinetics of La<sub>2</sub>O<sub>3</sub>-CaO-modified CeO<sub>2</sub> catalyst in a Multiphysics micromodel to predict CH<sub>4</sub> conversion rate and C<sub>2</sub> yield in a new plug-flow membrane reactor. The performance of the reactor is then compared with a fixed-bed reactor counterpart to show the advantages of the new technology.

### Types of Reactors Simulated

In this study, we simulate a tubular plug-flow membrane reactor and a fixed-bed reactor for model/experiment coupling and comparison purposes. The working principle of each reactor is schematically illustrated in Figs. 1a and 1b. In the membrane reactor (Fig. 1c), the CTM consists of three phases: Sm-doped  $\text{CeO}_2$  as the solid oxide (SO) phase, molten eutectic  $\text{Li}_2\text{CO}_3\text{-Na}_2\text{CO}_3$  as the molten carbonate (MC) phase, and the  $\text{LiNiO}_2$  (LNO) phase formed in situ between  $\text{NiO}$  and MC working as the electron conducting phase.<sup>20</sup> With such a membrane composition, only  $\text{CO}_2$  and  $\text{O}_2$  in the flue gas can permeate through the membrane to react with methane on the other side. The central passage of the plug-flow membrane reactor is filled with  $\text{La}_2\text{O}_3\text{-CaO}$ -modified  $\text{CeO}_2$  catalyst having a 34% porosity. A pure stream of methane is fed into the reactor through the catalyst bed, while a mixture of  $\text{CO}_2$ ,  $\text{O}_2$ , and  $\text{N}_2$  as a mockup of the flue gas from power plants is fed along the outer surface of the reactor. During operation, the CTM gradually adds  $\text{CO}_2$  and  $\text{O}_2$  into the methane chamber under the gradient of chemical potentials of  $\text{CO}_2$  and  $\text{O}_2$ . There are eleven catalytic reactions (solid line in the reaction network shown in Fig. 1d) on the surface and one bulk reaction in the gas phase (dashed line in the same plot) considered inside the reactor (methane chamber). The corresponding reaction kinetics have been listed in Table I. Ethylene is the product in the outlet. A 2D axial symmetrical model was built to simulate the performance of a membrane reactor coupled with a catalyst bed, shown in Fig. 1e.  $r$  axis represents the radius direction and  $z$  axis is the longitudinal direction of the tubular reactor. The gas species is flowing in the  $z$  direction, entering from the left and exiting from the right.

In the fixed-bed reactor (Fig. 1f), the composition, diameter, and length, as well as the porosity of the catalyst bed, and the inlet  $\text{CH}_4$  flow velocity are the same as the membrane reactor. There are, however, two major differences in the fixed-bed reactor modeling compared to the membrane reactor: (1) a mixture of  $\text{CH}_4$  and  $\text{CO}_2/\text{O}_2$  is co-fed at the inlet of the reactor; (2) there is only one computational domain for the catalyst bed.

### Mathematical Models

In this section, we give more details about the mathematical models used to simulate both OCM reactors. The reaction kinetics of OCM on  $\text{La}_2\text{O}_3\text{-CaO}$ -modified  $\text{CeO}_2$  catalyst involves many species. A 10-step kinetic model was first proposed by Stansch et al.<sup>21</sup> for  $\text{O}_2$  OCM. It describes the differential rates of formation of different species under a wide range of operating conditions ( $1 < p_{\text{O}_2} < 20\text{kPa}$ ,  $10 < p_{\text{CH}_4} < 95\text{kPa}$ ,  $973 < T < 1228\text{ K}$ ). The kinetic model includes thermal cracking, steam reforming and water gas shift reactions, see Table I. The kinetic parameters are estimated based on experimental data obtained from a microcatalytic fixed bed reactor in the model and experiment coupling section.<sup>1</sup> The reaction rate equations are either in the Hougen-Watson type (reaction 1–6) or the Power-law type (reaction 7–10). In addition, we also considered direct reaction between  $\text{CH}_4$  and  $\text{CO}_2$  as reaction (11) with the experimental data from Wang et al.<sup>22</sup>

Table II lists the governing equations and boundary conditions in both the membrane and the catalyst bed. The model was solved using commercial finite element package Comsol 5.4, Mathematics/The General Form PDE interface. A mapped mesh with 3500 linear quadrilateral elements was used in discretization. According to the definition of our previous work,<sup>23</sup> the membrane consists of three phases: molten carbonate phase transporting carbonate ions, mixed oxide and electron conducting phase transporting both oxide-ions and electrons, and the LNO phase transporting electrons only. Therefore, there are four charge conservation equations in the membrane domain. The details of the governing equations and boundary conditions can be found in our previous work.<sup>23</sup> In the

catalyst bed, the diffusion and convection of the gas species are described by transport of dilute species in porous media. The reaction kinetics at the catalyst surface or the bulk are given in Table III. The velocity of the gas stream is assumed to be constant.

To evaluate the overall performance of the OCM reactors, three metrics are used: C2 yield ( $Y_{\text{C}_2}$ ), selectivity ( $S_{\text{C}_2}$ ), and  $\text{CH}_4$  conversion rate ( $C_{\text{CH}_4}$ ), which are calculated by:

$$Y_{\text{C}_2} = S_{\text{C}_2} \cdot C_{\text{CH}_4} \quad [1]$$

$$S_{\text{C}_2} = \frac{[2 \times (J_{\text{C}_2\text{H}_4,\text{out}} - J_{\text{C}_2\text{H}_4,\text{in}}) + 2 \times (J_{\text{C}_2\text{H}_6,\text{out}} - J_{\text{C}_2\text{H}_6,\text{in}})]}{J_{\text{CH}_4,\text{in}} - J_{\text{CH}_4,\text{out}}} \quad [2]$$

$$C_{\text{CH}_4} = \frac{J_{\text{CH}_4,\text{in}} - J_{\text{CH}_4,\text{out}}}{J_{\text{CH}_4,\text{in}}} \quad [3]$$

**Model and experiment coupling.**—Parameters of the CTM and the catalyst bed were tuned to fit each model separately with each set of experimental data. The 1D CTM model was fitted by experimental data from the button cell of our previous work.<sup>23</sup> Here, we extend the model from 1D<sup>21</sup> to 2D. Therefore, in Fig. 2a, we compare the  $\text{CO}_2$  fluxes calculated by both 1D and 2D models with experimental data and found good agreement among the three sets of data. So, we think the membrane parameters extracted from experimental button cell data can be used to simulate the performance of a pilot-scale membrane.

Model and experiment coupling of the  $\text{O}_2$  OCM catalyst bed is done by optimization of the C2 yield and  $\text{CH}_4$  conversion rate to fit their experimental data obtained from a micro-catalytic fixed-bed reactor with  $\text{La}_2\text{O}_3\text{/CaO}$  catalyst as reported by Stansch<sup>25,24</sup>; the results are shown in Figs. 2b and 2c. With the obtained 10-step reaction kinetic parameters listed in Table III, an actual micro-catalytic reactor shown in Fig. 1 is simulated. Model and experiment coupling of reaction 11 with  $\text{CaO}$ /modified  $\text{CeO}_2$  catalyst for  $\text{CO}_2$  direct oxidation of  $\text{CH}_4$  is done with experimental data<sup>22</sup>; the results are shown in Fig. 2d.

After the model and experiment coupling, a composite catalyst  $\text{La}_2\text{O}_3\text{/CaO}$ -modified  $\text{CeO}_2$  catalyst for both  $\text{O}_2$  OCM and  $\text{CO}_2$  OCM has been used in the model as the catalyst bed. It is then used to simulate the performance of a membrane reactor and a fixed-bed reactor with the same catalyst bed dimensions and operating conditions given in Table IV. The material properties in the table are obtained from the fitting process.

### Results and Discussion

In this section, we compare the simulated performance of a membrane reactor and a fixed-bed reactor with the same catalyst bed and operating conditions. The operating temperature is varied between 973 K and 1103 K. The purpose of this study is to demonstrate the improved performance with the new membrane reactor over the state-of-the-art fixed-bed reactor.

**Fixed-bed reactor.**—Figure 3 shows 2D axial symmetric molar fraction profiles of gas species in a co-fed fixed-bed reactor under 1103 K. Note that the 2D domain will be rotated around its vertical orientation to form a cylinder in 3D.  $\text{CH}_4$  and  $\text{CO}_2/\text{O}_2$  streams are co-flowing from the top inlet to the bottom outlet of the cylindrical catalyst bed. To ensure a fair comparison,  $\text{CO}_2/\text{O}_2$  flowrates are the same as their equivalent flowrates permeated through the membrane in the membrane reactor. The wall of the container is under zero-flux boundary condition. It can be seen that  $\text{CH}_4$  and  $\text{CO}_2/\text{O}_2$  have been continuously converted to  $\text{CO}$ ,  $\text{C}_2\text{H}_6$ ,  $\text{C}_2\text{H}_4$ ,  $\text{H}_2\text{O}$  and  $\text{H}_2$ , as the stream move toward the outlet (bottom) of the tubular reactor.

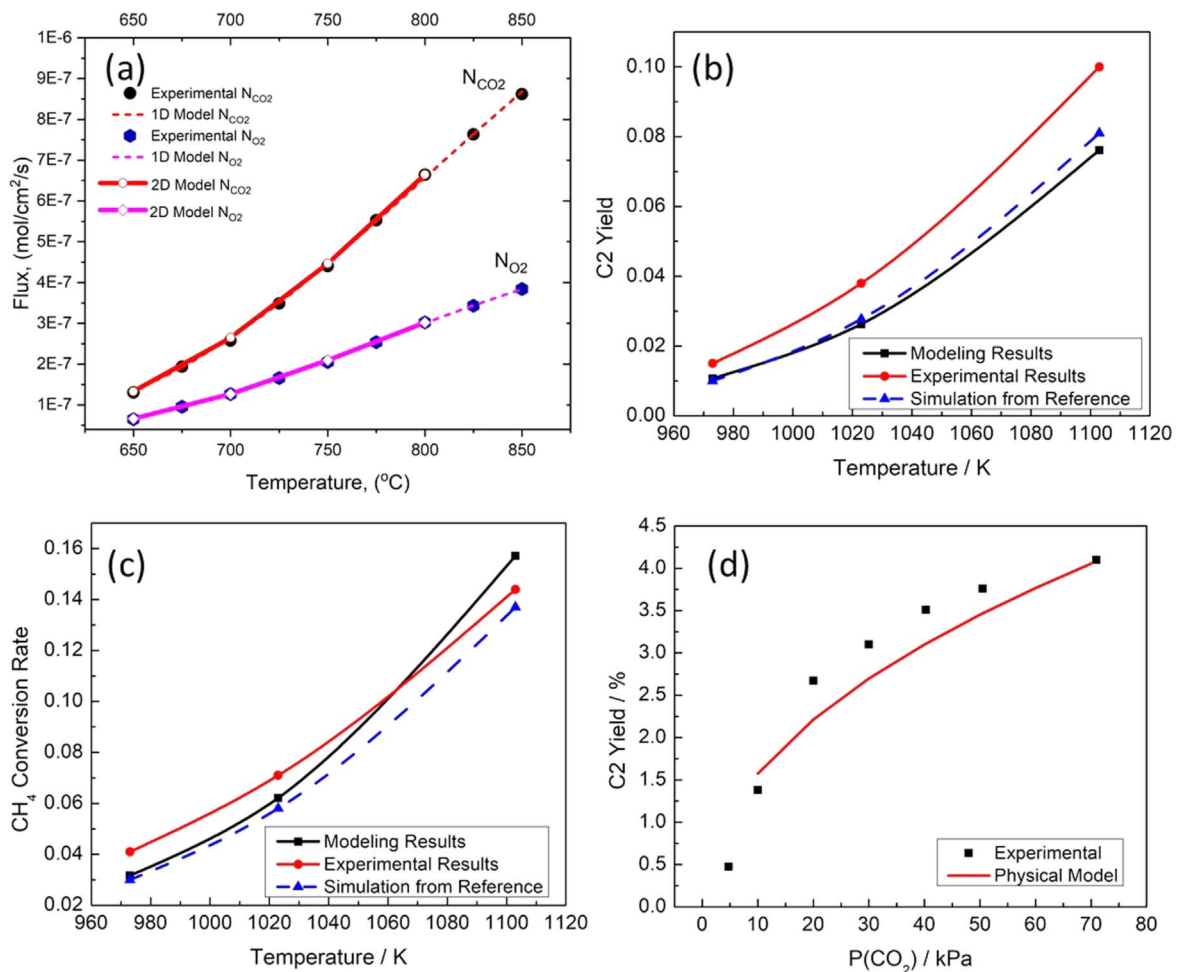
To show the gas species molar fraction profiles along the flow direction under different temperatures quantitatively, we plotted

**Table II.** Governing equations and boundary conditions (B. C.) for different domains.

Physics	Governing Eq.	B.C. @ Feed Side (Outer surface)	B.C. @ Sweep Side (Inner surface)
Membrane			
Oxygen vacancy conservation in SO phase	$\nabla \bullet J_V = -\frac{(1-\varepsilon)}{\tau_{SO}} \left( Z_V F D_V \nabla^2 C_V + \frac{Z_V^2 F^2 D_V C_V}{RT} \nabla^2 \phi_{SO} \right) = 0$	$\phi_{SO,0} = \frac{RT \left( \ln \frac{P_{CO_2,0}}{p_0} \frac{C^0}{C_V} \right) - \beta}{F Z_V}$	$J_V + J_n + J_C + J_{n,LNO} = 0$
Molten carbonate ion conservation in MC phase	$\nabla \bullet J_C = -\frac{\varepsilon}{\tau_{MC}} \sigma_C \nabla^2 \phi_{MC} = 0$	$\phi_{MC}(x=0) = 0$	$\phi_{MC,L} = \frac{RT \left( \ln \frac{P_{CO_2,L}}{p_0} \frac{C^0}{C_V} \right) - \beta}{F Z_C} - \frac{Z_V \phi_{SO,L}}{Z_C}$
Electron/hole conservation in SO phase	$\nabla \bullet J_n = -\frac{(1-\varepsilon)}{\tau_{SO}} \left( Z_n F D_n \nabla^2 C_n + \frac{Z_n^2 F^2 D_n C_n}{RT} \nabla^2 \phi_{SO} \right) = 0$	$C_n(0) = K_T^{1/2} C_v^{1/2} P_{O_2,0}^{1/2}$	$C_n(L) = K_T^{1/2} C_v^{1/2} P_{O_2,L}^{1/2}$
Electron conservation in metal phase	$\nabla \bullet J_{e,LNO} = -V_{LNO} (\sigma_{e,LNO} \nabla^2 \phi_{LNO}) = 0$	$Z_V C_V + Z_n C_n + Z_D C_D = 0$ $\phi_{LNO,0} = \frac{\chi}{2Z_e F} - \frac{RT}{2Z_e F} \ln \frac{P_{CO_2,0}}{p_0} \left( \frac{P_{O_2,0}}{p_0} \right)^{0.5}$	$Z_V C_V + Z_n C_n + Z_D C_D = 0$ $\phi_{LNO,L} = \frac{\chi}{2Z_e F} - \frac{RT}{2Z_e F} \ln \frac{P_{CO_2,L}}{p_0} \left( \frac{P_{O_2,L}}{p_0} \right)^{0.5} + \frac{Z_C}{2Z_e} \phi_{MC,L}$
Catalyst Bed			
Transport of diluted species in porous media	$\nabla \bullet N_i + \mathbf{u} \bullet \nabla c_i = R_i$	Inflow (Left inlet): $c_i = c_{0,i}$	Outflow (Right outlet): $\mathbf{n} \bullet D_i \nabla c_i = 0$
	$N_i = -D_i \nabla C_i$		

**Table III.** Kinetic parameters for catalytic and bulk reactions.<sup>21</sup>

Index	$k_{0j} \text{ mol}^{-1} \times \text{g}^{-1} \times \text{s}^{-1} \times \text{Pa}^{-(m+n)}$	$E_{a,j}$	$K_{j,\text{CO}_2}$	$\Delta H_{\text{ad},\text{CO}_2} \text{ kJ mol}^{-1}$	$K_{\text{O}_2} \text{ Pa}^{-1}$	$\Delta H_{\text{ad},\text{O}_2}$	$m_j$	$n_j$
1	$0.2 \times 10^{-5}$	48	$0.25 \times 10^{-12}$	-175	—	—	0.24	0.76
2	23.2	182	$0.83 \times 10^{-13}$	-186	$0.23 \times 10^{-11}$	-124	1	0.4
3	$0.52 \times 10^{-6}$	68	$0.36 \times 10^{-13}$	-187	—	—	0.57	0.85
4	$0.11 \times 10^{-3}$	104	$0.4 \times 10^{-12}$	-168	—	—	1	0.55
5	0.17	157	$0.45 \times 10^{-12}$	-166	—	—	0.95	0.37
6	0.06	166	$0.16 \times 10^{-12}$	-211	—	—	1	0.96
7	$1.2 \times 10^7$	226	—	—	—	—	—	—
8	$9.3 \times 10^3$	300	—	—	—	—	0.97	0
9	$0.19 \times 10^{-3}$	173	—	—	—	—	1.0	1.0
10	$0.26 \times 10^{-1}$	220	—	—	—	—	1.0	1.0
11	$1.8 \times 10^{-7}$	140	—	—	—	—	2	0.5

**Figure 2.** (a) CO<sub>2</sub> flux of the membrane. O<sub>2</sub> OCM for the fixed catalyst bed: (b) C2 yield; (c) CH<sub>4</sub> conversion rate, blue curve is from.<sup>24</sup> (d) CO<sub>2</sub> OCM for the fixed catalyst bed, experimental data is from.<sup>22</sup>

their profiles along the  $z$ -axis of the cylindrical catalyst bed, see Fig. 4. Since CH<sub>4</sub> molar fraction is much higher than the rest of the species, it is not plotted here. CH<sub>4</sub> conversion rate will be discussed in section “Performance comparison”. The inlet corresponds to  $z = 0$  mm and outlet is at  $z = 400$  mm. The following trends are observed: (1) The molar fraction of C<sub>2</sub>H<sub>6</sub> increases with temperature from 973 K to 1023 K, and then decreases sharply toward 1103 K. (2) The produced molar fraction of C<sub>2</sub>H<sub>4</sub> surpassed that for C<sub>2</sub>H<sub>6</sub> at 1103 K. (3) The molar fraction of H<sub>2</sub>O rises sharply first and then stays flat around 0.09 as temperature increases. (4) CO molar

fraction is below 0.02 for all three cases. (5) O<sub>2</sub> molar fraction decreases fast with temperature and then becomes depleted at 1103 K. (6) CO<sub>2</sub> molar fraction profiles are quite stable for the lower temperatures but started to decrease largely at 1103 K.

To understand the molar fraction profiles of all species and its relationship with the catalytic and bulk reactions in the fixed-bed reactor, the reaction rates of all 11 reactions listed in Table I are plotted along the  $z$ -axis of the reactor. There are 10 catalytic reactions (1–6, 8–11) with a unit of mol/kg/s, and 1 bulk reaction (7) with a unit of mol/m<sup>3</sup>/s. The catalytic reactions are plotted

**Table IV.** Parameters and operating conditions for both fixed-bed and membrane reactors.

Parameter	Value	References
Common Parameters for Both Reactors		
Reactor length	0.4 [m]	24
Reactor diameter	0.018 [m]	
Operating temperature	973–1103 [K]	
Sweep gas composition	99.3% CH <sub>4</sub>	
CH <sub>4</sub> stream velocity	0.39 [m s <sup>-1</sup> ]	
CO <sub>2</sub> diffusivity	1.39 × 10 <sup>-4</sup> [m <sup>2</sup> s <sup>-1</sup> ]	26
CO diffusivity	1.45 × 10 <sup>-4</sup> [m <sup>2</sup> s <sup>-1</sup> ]	
O <sub>2</sub> diffusivity	1.52 × 10 <sup>-4</sup> [m <sup>2</sup> s <sup>-1</sup> ]	
CH <sub>4</sub> diffusivity	1.57 × 10 <sup>-4</sup> [m <sup>2</sup> s <sup>-1</sup> ]	
C <sub>2</sub> H <sub>6</sub> diffusivity	1.31 × 10 <sup>-4</sup> [m <sup>2</sup> s <sup>-1</sup> ]	
C <sub>2</sub> H <sub>4</sub> diffusivity	1.37 × 10 <sup>-4</sup> [m <sup>2</sup> s <sup>-1</sup> ]	
H <sub>2</sub> O diffusivity	1.95 × 10 <sup>-4</sup> [m <sup>2</sup> s <sup>-1</sup> ]	
H <sub>2</sub> diffusivity	6.20 × 10 <sup>-4</sup> [m <sup>2</sup> s <sup>-1</sup> ]	
Membrane Reactor Specific Parameters		
Membrane thickness	0.2 [mm]	5
Feed gas composition	15% CO <sub>2</sub> : 10% O <sub>2</sub> : 75% N <sub>2</sub>	5
Sweep gas composition	99.3% CH <sub>4</sub>	—
LNO conductivity	$\ln \sigma = 5.8456 - \frac{463.9}{T}$ [S m <sup>-1</sup> ]	5
Molten Carbonate conductivity	$\sigma = -4.6866 + 8.533 \cdot 10^{-3} \cdot T - 1.325 \cdot 10^{-6} \cdot T^2$	27
SDC20 ionic conductivity	$\sigma_i = \frac{Z_i^2 F^2 D_i C_i}{RT} = Z_i^2 F \mu_i C_i$	28, 29
SDC20 electronic conductivity	$\log_{10}(\mu_{i,10} T) = 2.4656 - 3.40416 \cdot \frac{1000}{T}$ $\log_{10}(\mu_{i,20} T) = 2.36515 - 3.56931 \cdot \frac{1000}{T}$ $\log_{10}(\mu_{e,10} T) = 4.1943 - 4.30072 \cdot \frac{1000}{T}$ $\log_{10}(\mu_{e,20} T) = 2.63204 - 2.6264 \cdot \frac{1000}{T}$	28, 29
Tortuosity of the solid oxide phase	2.5	23
Tortuosity of the molten carbonate phase	$\ln \tau_{MC} = -9.2167 + \frac{11234.4}{T}$	23
Tortuosity of the LNO phase	$\tau_{LNO} = 0.5768 + 0.0055 \cdot T$	23
Volume fraction of molten carbonate	0.5	23
Volume fraction of LNO phase	0.01	23
Fixed-Bed Reactor Specific Parameters		
Inlet gas composition	8.7%CO <sub>2</sub> , 4.3%O <sub>2</sub> , 87% CH <sub>4</sub>	24

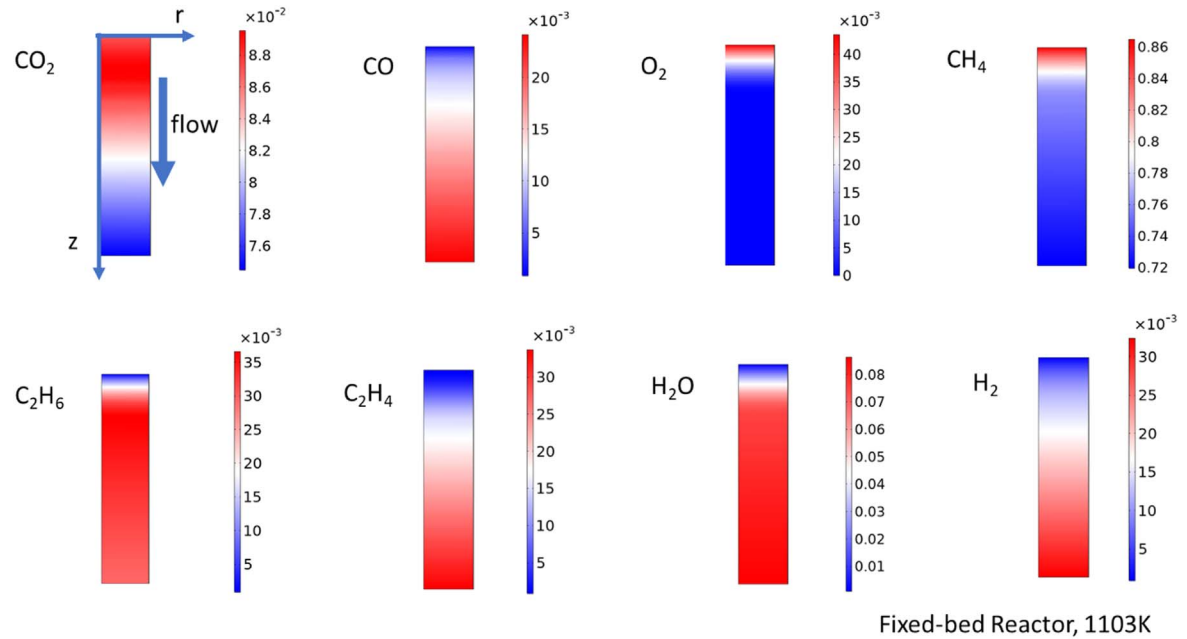
against the left *y*-axis in Fig. 5 and the bulk reaction is plotted against the right *y* axis. Reaction 3 (producing undesirable C1), and reaction 2 and 11 (producing desirable C2) are the most significant reactions. Reaction 3 shows a decreasing trend along the *z* axis and decreases faster at higher temperatures. The bulk reaction 7 converts C<sub>2</sub>H<sub>6</sub> to C<sub>2</sub>H<sub>4</sub> and its reaction rate is enhanced by higher temperatures. Its profile in the *z* axis direction is correlated to the reactant C<sub>2</sub>H<sub>6</sub> molar fraction. Even though reactions 2 and 11 (C2 reaction) and reaction 7 (from C<sub>2</sub>H<sub>6</sub> to C<sub>2</sub>H<sub>4</sub>) have been significantly enhanced at 1103 K, reactions 5 (convert C<sub>2</sub>H<sub>6</sub> to C<sub>2</sub>H<sub>4</sub>) and 6 (convert C<sub>2</sub>H<sub>4</sub> to CO) have also been facilitated, which prevents further increase of C2 product in Fig. 4.

**Membrane reactor.**—Different from the fixed-bed reactor, in the membrane reactor, pure CH<sub>4</sub> is fed at the inlet, while CO<sub>2</sub>/O<sub>2</sub> is gradually added into the reactor through the CTM. The catalyst bed of the membrane reactor is the same as that for the fixed-bed reactor. The CH<sub>4</sub> inflow velocity is the same as that for the fixed-bed reactor. The flux of CO<sub>2</sub>/O<sub>2</sub> is determined by the in situ CO<sub>2</sub>/O<sub>2</sub> partial pressure gradients across the membrane and varies along the *z*-axis. Their overall flux is the same as that at the inlet of the fixed bed reactor.

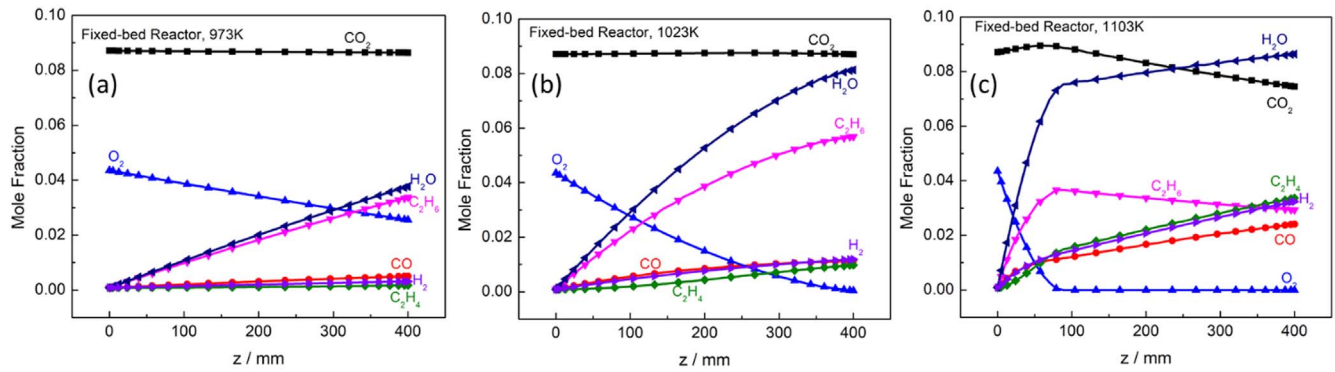
Figure 6 shows 2D axial symmetric gas species molar fraction profiles along the membrane reactor at 1103 K, from which we can see that: (1) CO<sub>2</sub> and O<sub>2</sub> are gradually added into the reactor through the wall of the membrane reactor. (2) CH<sub>4</sub> is consumed in the bulk of the reactor and there is a significant variation along the radial direction since there are more abundant O<sub>2</sub> and CO<sub>2</sub> permeated from the membrane at the inner surface. (3) Both C<sub>2</sub> products (C<sub>2</sub>H<sub>6</sub> and C<sub>2</sub>H<sub>4</sub>) are produced in the bulk of the reactor, and their molar fraction are slightly higher along the membrane inner surface. (4) Large amounts of H<sub>2</sub>O and H<sub>2</sub> are also produced at the outlet of the reactor. (5) CO molar fraction is the lowest in the reactor.

Figure 7 shows the molar fraction variations along the membrane inner surface in the *z*-axis direction. Compared to their counterparts' plots for fixed-bed reactors, there are three major differences: (1) C<sub>2</sub> (C<sub>2</sub>H<sub>4</sub> and C<sub>2</sub>H<sub>6</sub>) molar fractions are higher for the membrane reactor, especially at higher temperature 1103 K. (2) H<sub>2</sub>O product mole fraction is twice as high compared with that for the fixed-bed reactor. (3) CO<sub>2</sub> molar fraction becomes dominant species in the product stream, indicating higher CH<sub>4</sub> oxidation rate. As temperature increases, CO<sub>2</sub> domination has been weakened by H<sub>2</sub>O.

Figure 8 further confirms the enhanced reaction kinetics for more desirable reactions, such as reactions 2 and 11 (producing C<sub>2</sub>H<sub>6</sub>),



**Figure 3.** 2D axial symmetric gas species molar fraction profiles in the fixed-bed reactor under 1103 K. (Gas is flowing from the top inlet to the bottom outlet).



**Figure 4.** Molar fractions of gas species in the co-fed fixed-bed reactor along the  $z$  axis under (a) 973 K; (b) 1023 K; (c) 1103 K.

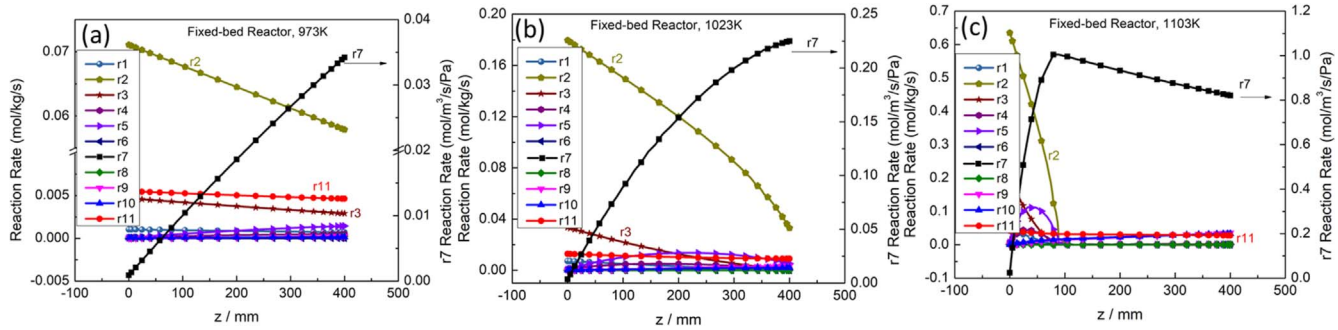


**Figure 5.** Reaction rates in the fixed-bed reactor along the  $z$  axis under (a) 973 K; (b) 1023 K; (c) 1103 K.

and reaction 5 (producing  $\text{C}_2\text{H}_4$ ), especially towards the outlet of the reactor. Therefore, elongating the reactor in the flow direction could further improve its performance by enhancing  $\text{CO}_2/\text{O}_2$  OCM reaction.

**Performance comparison.**—To compare the overall performance of the two different OCM reactors,  $\text{C}_2$  yield and selectivity,

as well as  $\text{CH}_4$  conversion rate from Eq. 1–3 are plotted against operating temperature in Fig. 9. One can see that (1) for the fixed bed reactor,  $\text{C}_2$  yield reaches the maximum of  $\sim 15\%$  around 1023 K, whereas for the membrane reactor, it continues to increase as the temperature increases; (2)  $\text{C}_2$  selectivity for the membrane reactor remains above 93% while that for the fixed-bed falls under 91% at 1103 K; (3) The  $\text{CH}_4$  conversion rate for the membrane reactor is

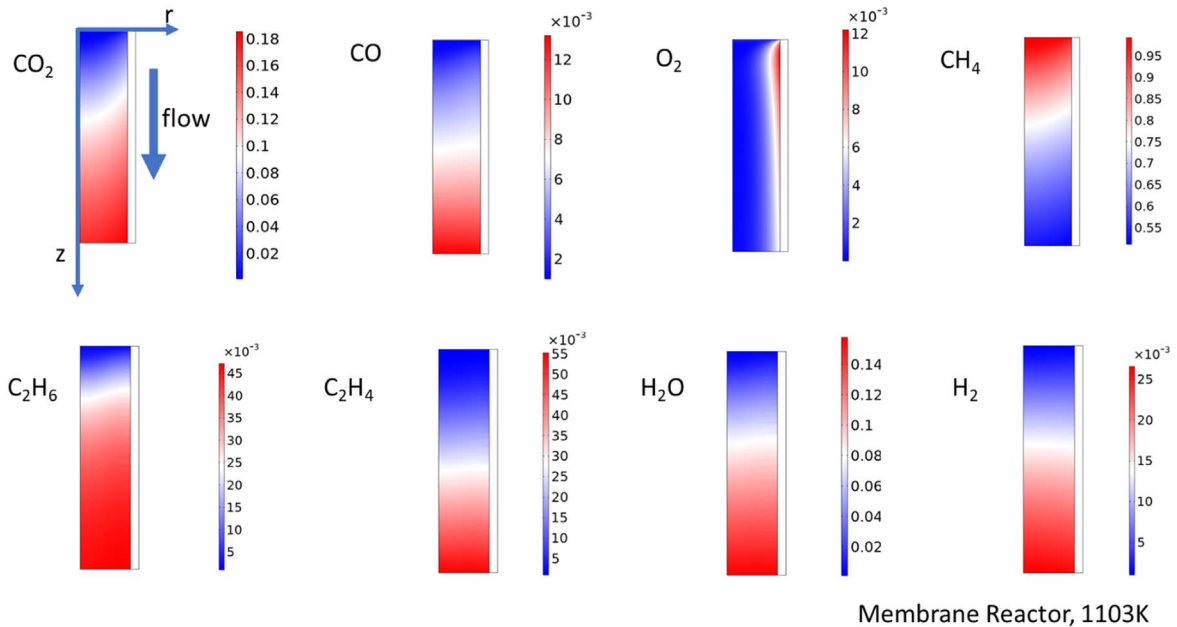


**Figure 6.** 2D axial symmetric gas species molar fraction profiles in the membrane reactor under 1103 K. (Gas is flowing from the top inlet to the bottom outlet).

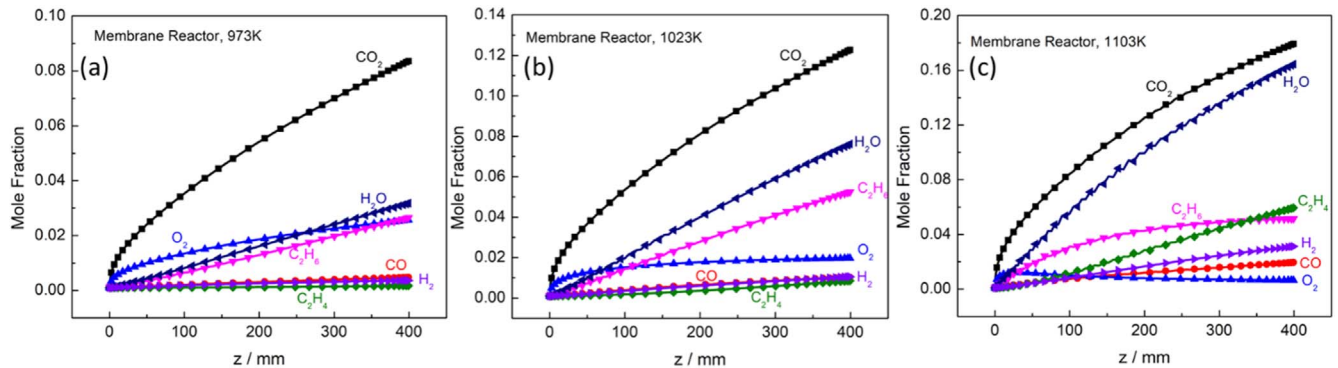


**Figure 7.** Molar fractions of gas species in the membrane reactor along the  $z$  axis under (a) 973 K; (b) 1023 K; (c) 1103 K.

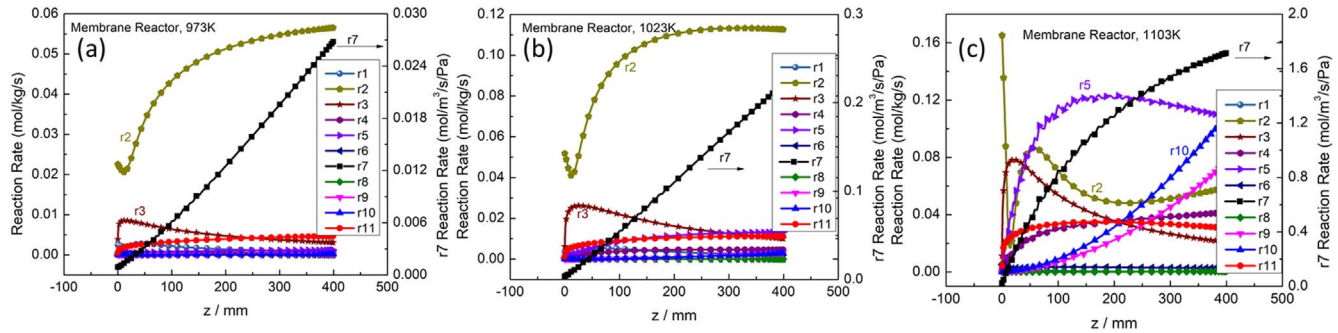


**Figure 8.** Reaction rates in the membrane reactor along the  $z$  axis under (a) 973 K; (b) 1023 K; (c) 1103 K.

more than twice that of the fixed-bed reactor at 1103 K. At the same time, a significant amount of CO<sub>2</sub> has been captured in the membrane reactor from the flue gas.

In Fig. 10a, CO<sub>2</sub>/O<sub>2</sub> flux along the membrane inner surface in the  $z$ -axis direction is plotted. It increases with temperature but decreases exponentially along the  $z$ -axis from the inlet to the outlet at a given temperature. At the inlet, large amount of CO<sub>2</sub>/O<sub>2</sub> is needed to convert CH<sub>4</sub> to C<sub>2</sub> products; as the stream approaches the outlet, CO<sub>2</sub>/O<sub>2</sub> concentration in the membrane reactor increases,

which reduces the driving force for the chemical potential driven diffusion process and leads to reduced CO<sub>2</sub>/O<sub>2</sub> flux. In Fig. 10b, CH<sub>4</sub> molar fraction is plotted against the  $z$ -axis. It decreases along the  $z$ -axis from the inlet to the outlet. The CH<sub>4</sub> molar fraction decreases more abruptly along the  $z$  axis in the membrane reactor than that in the fixed-bed reactor, which is consistent with the CH<sub>4</sub> conversion rate shown in Fig. 9c.

The comparison results in Figs. 9 and 10 indicate that the membrane reactor shows improved performance under higher

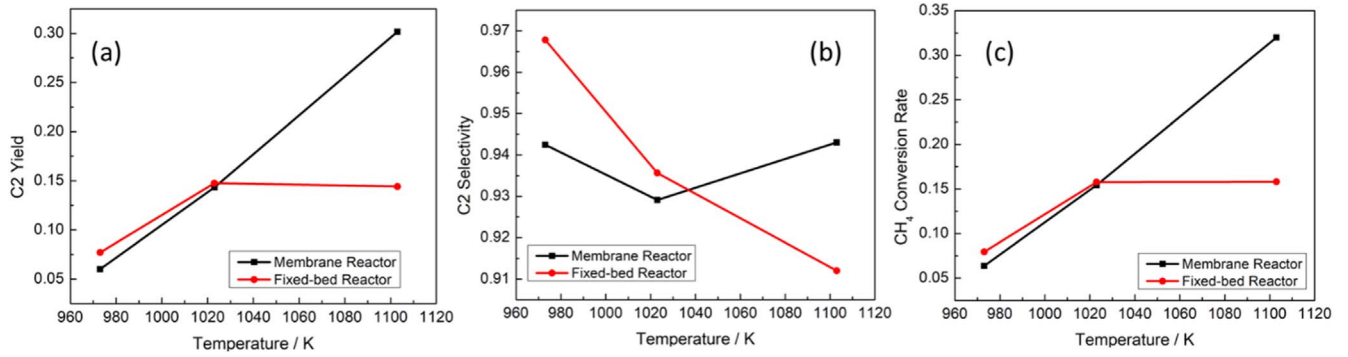


**Figure 9.** Performance comparison between membrane and fixed-bed reactors: (a) C2 yield; (b) C2 selectivity; (c) CH<sub>4</sub> conversion rate.

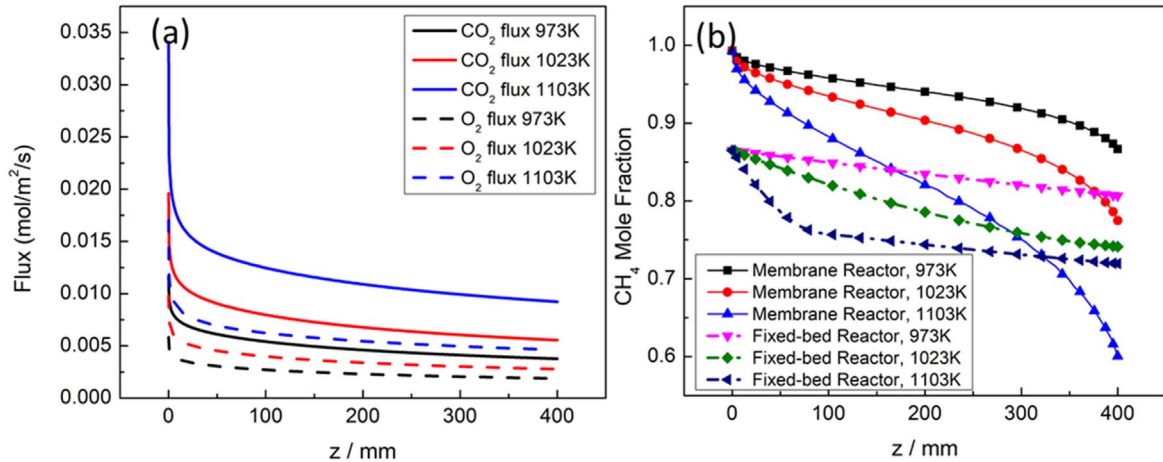


**Figure 10.** (a) CO<sub>2</sub> flux along the gas/membrane interface in the membrane reactor; (b) CH<sub>4</sub> molar fraction comparison between membrane and fixed-bed reactors.

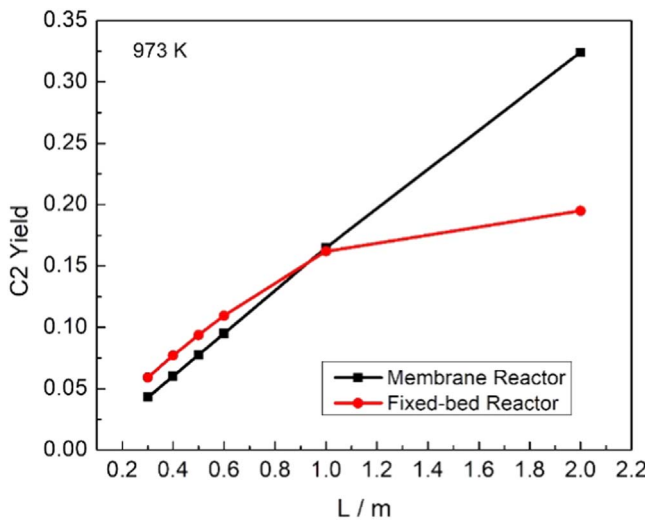


**Figure 11.** C2 Yield as a function of reactor length.

temperatures in terms of C2 yield/selectivity and CH<sub>4</sub> conversion rate. However, in practical operation a lower operating temperature is preferred to maintain a longer lifetime of the reactor. An alternative solution to improve the reactor performance at lower temperatures is to lengthen the reactors. The fixed-bed reactor has a well-known limitation in C2 yield. As shown in Fig. 11, C2 yield is plateaued at 20% with a reactor length higher than 1.4 m. But for the membrane

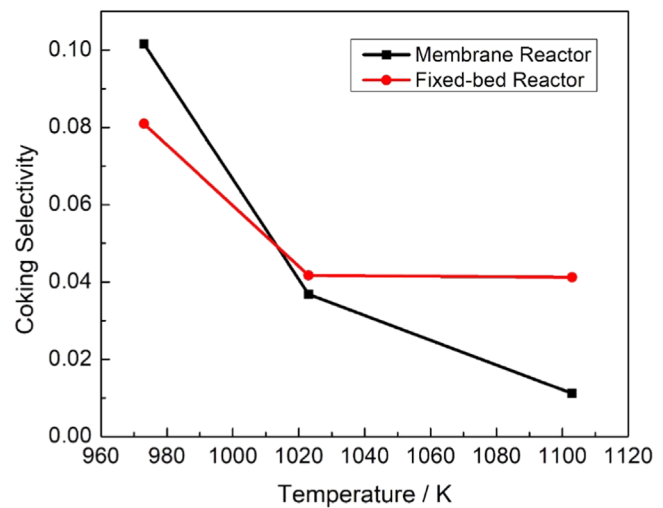


**Figure 12.** Coking Selectivity as a function of operating temperature.

reactor, as the length increases, C2 yield linearly increases and could reach as high as 32% with a reactor length of 2 m. Therefore, it is economically beneficial to run a longer membrane reactor for combined CO<sub>2</sub> capture and OCM under lower temperatures.

**Coking resistance.**—Coke formation during OCM reaction is thermodynamically and kinetically favorable, particularly under controlled oxygen conditions to avoid over-oxidation, leading to

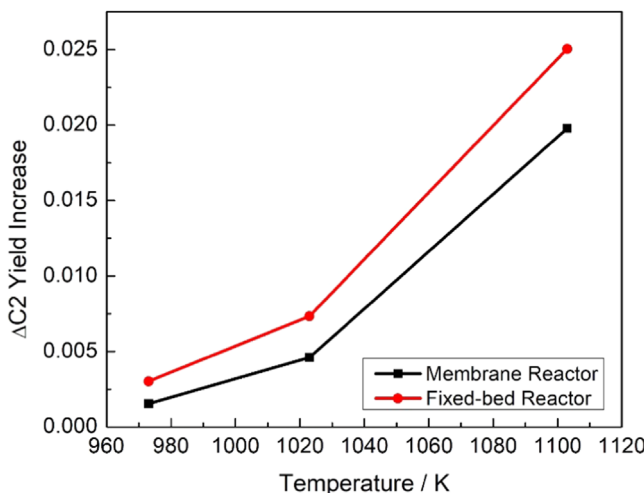


**Figure 13.** C2 yield increase for membrane reactor and fixed-bed reactor considering the OCM by  $\text{CO}_2$ .

loss of catalyst's activity via pore blockage, collapse of the catalyst support, or physical blockage of the tube in the fixed-bed reactor.<sup>30</sup> Coking is a major challenge for OCM to be commercially viable. The coking possibility of OCM in fixed-bed and membrane reactors is assessed by analyzing thermodynamic equilibrium with the gas composition calculated at the outlet of the reactors from the Comsol models under different temperatures. The results are shown in Fig. 12. Coking selectivity is defined as the moles of carbon produced divided by the moles of  $\text{CH}_4$  consumed. From the figure, we find that: (1) For the fixed bed reactor, coking selectivity decreases by more than 50% as temperature increases from 970 K to 1120 K, which is caused by fast reaction kinetics and abundance of  $\text{CO}_2/\text{H}_2\text{O}$  in the gas stream. (2) For the membrane reactor, a similar trend is observed but coking selectivity is slightly higher under low temperatures and much lower under high temperatures. Such improved coking resistance is due to the superior  $\text{CH}_4$  conversion rate of the membrane reactor under high temperatures. Therefore, we conclude that a higher operating temperature is beneficial to suppress coke formation. Along the gas flow direction, more oxidizers such as  $\text{CO}_2$  and  $\text{O}_2$  will be continually added into the reactor through the membrane, which will reduce coking.

**Direct  $\text{CO}_2$  oxidative coupling of methane.**—For the results presented in sections “Fixed-bed reactor”, “Membrane reactor”, and “Performance comparison”, direct oxidation of methane by  $\text{CO}_2$  (reaction 11) has been included. Compared to  $\text{O}_2$ -OCM (reaction 2),  $\text{CO}_2$ -OCM is more challenging given the nature of the stable  $\text{CO}_2$  molecule. However, using  $\text{CO}_2$  as an oxidizer for OCM has implications to mitigating  $\text{CO}_2$  emissions. In recent years, explorative studies on direct  $\text{CO}_2$ -OCM have been reported,<sup>30,31</sup> but with very low C2 yields (3%–6% depending on  $\text{CO}_2$  partial pressure in the gas mixture). In this study, we use the experimental data produced from  $\text{CaO}$ -modified  $\text{CeO}_2$  catalyst<sup>32</sup> to obtain the reaction kinetics parameter for reaction 11 in Table III and then incorporate the reaction into the models for fixed-bed reactor and membrane reactor. Referring to the C2 yield for OCM with  $\text{O}_2$  in Fig. 11, Fig. 13 shows that the maximum C2 yield increase vs temperature of direct  $\text{CH}_4$  oxidation by  $\text{CO}_2$ , which is similar for fixed-bed and membrane reactors, 2.5% for the fixed-bed reactor vs 2% for the membrane reactor at the highest temperature 1120 K and a reactor length of 0.4 m. For longer reactors, there will be more residence time for  $\text{CO}_2$  to react with  $\text{CH}_4$ . However, it is evident that  $\text{CO}_2$ -OCM contribution is marginal compared to  $\text{O}_2$ -OCM, regardless of the type of reactor. New catalysts would be needed to boost

$\text{CO}_2$ -OCM. As of now, the ability to capture  $\text{CO}_2$  and incremental addition of  $\text{O}_2$  into  $\text{CH}_4$  stream for OCM are the major advantages for the membrane reactors.

## Conclusions

In summary, we have developed a membrane reactor model to simulate the performance of a combined  $\text{CO}_2$  capture and  $\text{CH}_4$  oxidative coupling reaction. The model parameters are obtained by validating experimental data of C2 yield and  $\text{CH}_4$  conversion rate from a microcatalytic fixed-bed reactors, as well as  $\text{CO}_2$  flux in a lab-scale membrane. The results show that the membrane reactor has the following advantages over its counterpart fixed-bed reactor design. (1) The membrane reactor can overcome C2 yield limitation faced by the fixed bed reactor under higher operating temperatures or longer reactor length and achieve over 30% C2 yield. (2)  $\text{CO}_2$  molar fraction becomes dominant in the membrane reactor product stream, indicating a higher  $\text{CH}_4$  conversion rate. (3) Longer membrane reactor shows better coking resistance compared to its fixed-bed counterpart design. (4) Direct oxidation of  $\text{CH}_4$  by  $\text{CO}_2$  could only improve the C2 yield in the membrane reactor by 2%, suggesting that OCM is mainly carried out by  $\text{O}_2$ . We show that the membrane reactor with high intrinsic  $\text{CO}_2$  flux can become an efficient bifunctional device for simultaneous  $\text{CO}_2$  capture and  $\text{CH}_4$ -to- $\text{C}_2\text{H}_4$  conversion through OCM reaction. Further techno-economic analysis will be conducted to assess the commercialization potential of the technology in the future.

## Acknowledgments

This material is based upon work supported by the U.S. National Science Foundation under grant number CBET-1924095.

## ORCID

Kevin Huang  <https://orcid.org/0000-0002-1232-4593>  
Xinfang Jin  <https://orcid.org/0000-0002-3148-4904>

## References

1. L.-C. Lin et al., “In silico screening of carbon-capture materials..” *Nat. Mater.*, **11**, 633 (2012).
2. R. T. Pierrehumbert, “High levels of atmospheric carbon dioxide necessary for the termination of global glaciation.” *Nature*, **429**, 646 (2004).
3. H. R. Schultz, “Climate change and viticulture: a European perspective on climatology, carbon dioxide and UV-B effects.” *Aust. J. Grape Wine Res.*, **6**, 2 (2000).
4. P. Zhang, J. Tong, K. Huang, X. Zhu, and W. Yang, “The current status of high temperature electrochemistry-based  $\text{CO}_2$  transport membranes and reactors for direct  $\text{CO}_2$  capture and conversion.” *Prog. Energy Combust. Sci.*, **82**, 100888 (2021).
5. P. Zhang, J. Tong, and K. Huang, “Self-formed, mixed-conducting, triple-phase membrane for efficient  $\text{CO}_2/\text{O}_2$  capture from flue gas and in situ dry-oxy methane reforming.” *ACS Sustainable Chemistry & Engineering*, **6**, 14162 (2018).
6. P. Zhang, J. Tong, and K. Huang, “A study of low-cost NiO-MC dual-phase membrane for high-flux and selective electrochemistry-based  $\text{CO}_2$  capture.” *ECS Trans.*, **80**, 861 (2017).
7. J. H. Lunsford, “The catalytic oxidative coupling of methane.” *Angew. Chem. Int. Ed. Engl.*, **34**, 970 (1995).
8. D. Schwer, L. Meeckzo, and M. Baerns, “OCM in a fixed-bed reactor: limits and perspectives.” *Catal. Today*, **21**, 357 (1994).
9. S. Jaso, H. R. Godini, H. Arellano-Garcia, and G. Wozny, “Oxidative coupling of methane: reactor performance and operating conditions. computer aided.” *Chem. Eng.*, **28**, 6 (2010).
10. W. Kiatkittipong, T. Tagawa, S. Goto, S. Assabumrungrat, K. Silpasup, and P. Praserttham, “Comparative study of oxidative coupling of methane modeling in various types of reactor.” *Chem. Eng. J.*, **115**, 63 (2005).
11. A. Cruellas, T. Melchiori, F. Gallucci, and M. van Sint Annaland, “Advanced reactor concepts for oxidative coupling of methane..” *Catalysis Reviews*, **59**, 234 (2018).
12. A. L. Tonkovich, R. W. Carr, and R. Aris, “Enhanced C2 yields from methane oxidative coupling by means of a separative chemical reactor.” *Science*, **262**, 221 (1993).
13. S. Jašo et al., “Experimental investigation of fluidized-bed reactor performance for oxidative coupling of methane.” *J. Nat. Gas Chem.*, **21**, 534 (2012).
14. N. Yaghobi, M. Hamid, and R. Ghoreishi, “Oxidative coupling of methane in a fixed bed reactor over perovskite catalyst: a simulation study using experimental kinetic model..” *J. Nat. Gas Chem.*, **17**, 8 (2008).

15. F. M. Dautzenberg, J. C. Schlatter, J. M. Fox, J. R. Rostrup-Nielsen, and L. J. Christiansen, "Catalyst and reactor requirements for the oxidative coupling of methane." *Catal. Today*, **13**, 503 (1992).
16. S. Bhatia, C. Y. Thien, and A. R. Mohamed, "Oxidative coupling of methane (OCM) in a catalytic membrane reactor and comparison of its performance with other catalytic reactors." *Chem. Eng. J.*, **148**, 525 (2009).
17. W. Wang and Y. S. Lin, "Analysis of oxidative coupling of methane in dense oxide membrane reactors." *J. Membr. Sci.*, **103**, 219 (1995).
18. Y. K. Kao, L. Lei, and Y. S. Lin, "A comparative simulation study on oxidative coupling of methane in fixed-bed and membrane reactors." *Ind. Eng. Chem. Res.*, **36**, 3583 (1997).
19. A. M. Arinaga, M. C. Ziegelski, and T. J. Marks, "Alternative oxidants for the catalytic oxidative coupling of methane." *Angew. Chem. Int. Ed. Engl.*, **60**, 10502 (2021).
20. P. Zhang, J. Tong, and K. Huang, "A self-forming dual-phase membrane for high-temperature electrochemical CO<sub>2</sub> capture." *J. Mater. Chem. A*, **5**, 12769 (2017).
21. Z. Stansch, L. Mleczko, and M. Baerns, "Comprehensive kinetics of oxidative coupling of methane over the La<sub>2</sub>O<sub>3</sub>/CaO catalyst." *Ind. Eng. Chem. Res.*, **36**, 2568 (1997).
22. Y. Wang, Y. Takahashi, and Y. Ohtsuka, "Carbon dioxide as oxidant for the conversion of methane to ethane and ethylene using modified CeO<sub>2</sub> catalysts." *J. Catal.*, **186**, 160 (1999).
23. X. Li, K. Huang, and X. Jin, "Mathematical modeling of high-temperature multiphase solid/molten carbonate membranes for CO<sub>2</sub> capture." *J. Electrochem. Soc.*, **167**, 164512 (2020).
24. C. T. Tye, A. R. Mohamed, and S. Bhatia, "Modeling of catalytic reactor for oxidative coupling of methane using La<sub>2</sub>O<sub>3</sub>/CaO catalyst." *Chem. Eng. J.*, **87**, 49 (2002).
25. Z. Stansch, *Kinetics for Oxidative Coupling of Methane Process over La<sub>2</sub>O<sub>3</sub>/CaO catalyst*. (Ruhr-University Bochum, Bochum) (1995).
26. Kayode Coker, "Physical Properties of Liquids and Gases." *Ludwig's Applied Process Design for Chemical and Petrochemical Plants(Forth Edition)* (Gulf Professional Publishing, Burlington) Ch. 3, p. 103-132 (2007).
27. T. Kojima, Y. Miyazaki, K. Nomura, and K. Tanimoto, "Physical properties of molten Li<sub>2</sub>CO<sub>3</sub>-Na<sub>2</sub>CO<sub>3</sub>(52:48 mol%) and Li<sub>2</sub>CO<sub>3</sub>-K<sub>2</sub>CO<sub>3</sub>(62:38 mol%) containing additives." *J. Electrochem. Soc.*, **160**, H733 (2013).
28. A. Atkinson, "Chemically-induced stresses in gadolinium-doped ceria solid oxide fuel cell electrolytes." *Solid State Ionics*, **95**, 249 (1997).
29. S. Wang, T. Kobayashi, M. Dokuya, and T. Hashimoto, "Electrical and ionic conductivity of Gd-doped ceria." *J. Electrochem. Soc.*, **147**, 3606 (2000).
30. M. J. Ginsburg, J. Pina, T. E. Soh, and H. I. de Lasa, "Coke formation over a nickel catalyst under methane dry reforming conditions: thermodynamic and kinetic models." *Ind. Eng. Chem. Res.*, **44**, 4846 (2005).
31. X. Cai and Y. Hang Hu, "Advances in catalytic conversion of methane and carbon dioxide to highly valuable products." *Energy Science & Engineering*, **7**, 4 (2019).
32. Y. Zhang, Y. Cho, A. Yamaguchi, X. Peng, M. Miyachi, H. Abe, and T. Fujita, "CO<sub>2</sub> oxidative coupling of methane using an earth-abundant CaO-based catalyst." *Sci Rep.*, **9**, 15454 (2019).